THE ASTROPHYSICAL JOURNAL, 497:957–966, 1998 April 20

STATISTICAL PROPERTIES OF MAGNETIC ACTIVITY IN THE SOLAR CORONA

MANOLIS K. GEORGOULIS,[1,2] MARCO VELLI,[3] AND GIORGIO EINAUDI[2]
Received 1997 June 11; accepted 1997 November 26

ABSTRACT

The long-time statistical behavior of a two-dimensional section of a coronal loop subject to random magnetic forcing is presented. The highly intermittent nature of dissipation is revealed by means of magnetohydrodynamic (MHD) turbulence numerical simulations. Even with a moderate magnetic Reynolds number, intermittency is clearly present in both space and time. The response of the loop to the random forcing, as described either by the time series of the average and maximum energy dissipation or by its spatial distribution at a given time, displays a Gaussian noise component that may be subtracted to define discrete dissipative events. Distribution functions of both maximum and average current dissipation, for the total energy content, the peak activity, and the duration of such events are all shown to display robust scaling laws, with scaling indices δ that vary from $\delta \simeq -1.3$ to $\delta \simeq -2.8$ for the temporal distribution functions, while $\delta \simeq -2.6$ for the overall spatial distribution of dissipative events.

Subject headings: MHD — Sun: corona — Sun: flares — Sun: magnetic fields — turbulence

1. INTRODUCTION

The nature of energy release in the solar atmosphere remains one of the main unresolved problems in solar physics, although the correlation of activity with the intensity of photospheric magnetic fields seems beyond doubt. This has led to the idea that all coronal activity might be attributed to the dissipation of magnetic energy either previously stored in the corona or injected continuously via a flux of waves. Parker (1972) was the first to suggest that coronal heating could be the necessary outcome of an energy flux associated with the tangling of coronal field lines by photospheric flows. Parker (1983, 1988), Sturrock & Uchida (1981), Van Ballegooijen (1986), and Berger (1991), among others, further explored the dynamics caused by such random shuffling of magnetic field lines. Numerical simulations by Mikic, Schnack, & Van Hoven (1989) confirmed that this process causes a nonlinear cascade, leading to an exponential growth of local coronal currents. In subsequent papers, Parker clarified this scenario for coronal heating by introducing the terms "microflare" and then "nanoflare" to describe the dissipation of elementary coronal current sheets developed as a consequence of random footpoint motion (Parker 1989, 1991).

Observations of the statistical behavior of flaring activity (Lin et al. 1984; Dennis 1985; Vilmer 1987; Ramaty & Murphy 1987; Pick, Klein, & Trottet 1990; Crosby, Aschwanden, & Dennis 1993; Pearce, Rowe, & Yeung 1993; Biesecker 1994) have shown that distributions such as the number of flares as a function of total energy content, peak luminosity, or duration all display well-defined power laws, extending over several orders of magnitude, down to instrumental resolution. However, if such flaring activity is to account for coronal heating, it is necessary (Hudson 1991) for the power-law distribution at energies below the observed lower limit to switch to a significantly steeper scaling index (i.e., the number of nanoflares per interval of energy should significantly increase at low energies). Observations in the radio domain, which extend to the lowest recordable energies, indeed indicate that power-law behavior such as that observed in large flares continues to hold at much lower energies (although with different scaling indices; Mercier & Trottet 1997). Although the viability of the nanoflare scenario remains an open question observationally, it is important to remark that a comparison of the distributions of different observed "events" may have little meaning. For example, evidence for the existence of magnetic separatrices in some flaring regions (Démoulin, Hénoux, & Mandrini 1994) indicate that complexity beyond the simple random braiding of an axial field is necessary for certain classes of solar flares to occur. Stated differently, while for the low-energy activity associated with coronal heating the integrated energy flux from the photosphere is probably always comparable to the coronal dissipated power, in situ storage may be required for the larger flares, marking an important distinction in the dynamics, although not in the dissipation.

Although power-law behavior of energy release has been modeled successfully using cellular automaton models (SOC) of magnetic field instabilities (Lu & Hamilton 1991; Lu et al. 1993; Vlahos et al. 1995), there has been no evidence for such behavior coming either from MHD models or from the three-dimensional numerical simulations reported up to now (Mikic et al. 1989; Strauss 1993; Longcope & Sudan 1994; Galsgaard & Nordlund 1996; Hendrix & Van Hoven 1996). Based on the properties of the turbulence observed in three dimensions by Mikic et al. and Hendrix & Van Hoven, Einaudi et al. (1996) developed a two-dimensional model allowing for much larger integration times. Their simulations of magnetically forced MHD turbulence in a two-dimensional slab geometry, chosen to model a section of a coronal loop, demonstrated a number of results for the overall properties of energy release with varying resolution and Reynolds numbers; they demonstrated in particular that for a given random forcing, there is an increase in average dissipation with increasing Reynolds number as well as an increase of peak to average energy dissipation. Einaudi et al.'s (1996) simulations lasted about 600 poloidal Alfvén times, where the poloidal Alfvén time is given by the time it takes an Alfvén wave to cross the coronal loop given the typical value of the magnetic field in

[1] Section of Astrophysics, Astronomy, & Mechanics, Department of Physics, University of Thessaloniki, GR-54006 Thessaloniki, Greece.
[2] Dipartimento di Fisica, Università di Pisa, I-56100 Pisa, Italy.
[3] Dipartimento di Astronomia e Scienze dello Spazio, Università di Firenze, I-50125 Firenze, Italy.

the plane of the simulation, corresponding (as discussed in the following section) to about 10 times the transit time along the coronal loop.

Here we extend the simulations of Einaudi et al. (1996) to much longer times (4000 poloidal Alfvén times), since a very large data set is necessary to obtain reliable statistics. We will show that the spatial average of the dissipated power displays non-Gaussian statistics and that upon subtraction of the Gaussian component, a well-defined power law results for the number of "dissipative events" as a function of total dissipative energy; the same result holds for the local peak dissipation, as well as for the spatial distribution at a given time. This is to our knowledge the first direct connection between the behavior of a system described by MHD and the observational distribution of power release in the solar corona. Recently, Dmitruk & Gómez (1997) have presented a numerical simulation using the same model of a two-dimensional lattice, although with a lower spatial resolution (96 × 96), obtaining similar results.

The two-dimensional nature of our simulation might appear too restrictive and our previous statement too bold. From a computational point of view, having fields that depend on only two spatial variables is essential for simulations of the length that we have carried out. From a theoretical point of view, it is important to stress that in three-dimensional simulations of the Parker problem of random motion, the presence of a strong axial magnetic field makes variations in the axial direction very weak compared to those in a transverse plane and that in such cases the reduced MHD equations are an applicable model. We make a further approximation by substituting the advection of transverse magnetic and velocity fields in the axial direction via the axial magnetic field by a random forcing function, simplifying the problem to a completely two-dimensional one. The main limitation is then that no net magnetic helicity is injected in our system, and thus the energy storage capability is much reduced as compared to a truly three-dimensional system forced at the boundaries. We therefore stress that our model does not have much direct significance for the interpretation of real observed solar flares.

In § 2 we describe the basics of our numerical model. A statistical analysis of the resulting time series and the spatial configurations is presented in § 3, and in § 4 we summarize our results and discuss their impact on the interpretation of solar coronal phenomena.

2. MODEL DESCRIPTION

We model the cross section of a coronal loop threaded by a large axial magnetic field B_0 with footpoints at either end rooted in the photosphere. Denoting the axial direction by z, any disturbance originating in the photosphere propagates along z with the associated Alfvén velocity and gives rise to perpendicular magnetic and velocity fields $\boldsymbol{b}_\perp$ and $\boldsymbol{u}_\perp$. The time evolution of the perpendicular fields is well described by the reduced MHD equations (Strauss 1976, 1977):

$$\rho\left(\frac{\partial \boldsymbol{u}_\perp}{\partial t} + \boldsymbol{u}_\perp \cdot \nabla \boldsymbol{u}_\perp\right) = -\nabla_\perp\left(p + \frac{1}{2} b_\perp^2\right) + \boldsymbol{b}_\perp \cdot \nabla \boldsymbol{b}_\perp + B_0 \frac{\partial \boldsymbol{b}_\perp}{\partial z} + \nu \nabla_\perp^2 \boldsymbol{u}_\perp , \quad (1)$$

$$\frac{\partial \boldsymbol{b}_\perp}{\partial t} = \boldsymbol{b}_\perp \cdot \nabla \boldsymbol{u}_\perp - \boldsymbol{u}_\perp \cdot \nabla \boldsymbol{b}_\perp + B_0 \frac{\partial \boldsymbol{u}_\perp}{\partial z} + \eta \nabla_\perp^2 \boldsymbol{b}_\perp , \quad (2)$$

where ρ is the mass density, p is the plasma pressure, and ν and η are the collisional dissipation coefficients, the kinematic viscosity and the resistivity, respectively. These equations are valid in the limit of a small ratio of kinetic to magnetic pressure, a large loop-aspect ratio ($\epsilon \equiv l/L \ll 1$, L being the length of the loop and l being the minor radius of the loop), and a small ratio of poloidal to axial magnetic field ($b_\perp/B_0 \leq \epsilon$). The latter condition also ensures the incompressibility of plasma motion in the plane. As a consequence, the density, considered initially to be uniform, will remain so, allowing us to make use of the same units for velocity and magnetic fields via the normalization $b \rightarrow b/\rho^{1/2}$. Unless otherwise stated, we will implicitly assume that magnetic fields are measured in velocity units hereafter. The fields $\boldsymbol{b}_\perp$ and $\boldsymbol{u}_\perp$ depend on z, but they interact nonlinearly only in the perpendicular direction. The communication across planes at different z is provided by Alfvén waves propagating along the mean axial field, which carry the energy introduced in the loop by photospheric boundary motions. Since we are interested in the evolution of the perpendicular fields driven by such motions, the terms involved in the large-scale axial field in equations (1) and (2) may be considered as forcing terms that can be modeled according to our present knowledge of the photospheric driver. In other words, we can write

$$B_0\left(\frac{\partial \boldsymbol{u}_\perp}{\partial z}\right) = \boldsymbol{F}_m(x, y, t) , \quad (3)$$

$$B_0\left(\frac{\partial \boldsymbol{b}_\perp}{\partial z}\right) = \boldsymbol{F}_u(x, y, t) , \quad (4)$$

where $\boldsymbol{F}_m$ and $\boldsymbol{F}_u$ are unknown forcing functions. In a truly three-dimensional system, the fact that the plasma pressure is much smaller than the magnetic pressure implies that the magnetic field evolves following a series of force-free states in which the kinetic energy of the coronal plasma is substantially smaller than the magnetic free energy. This allows us to introduce a further simplification, which is to impose $\boldsymbol{F}_u = 0$ in our two-dimensional simulations. Moreover, the forcing term $\boldsymbol{F}_m$ of equation (3) can be rewritten in a more convenient way if we express equations (1) and (2) in terms of the vector potential $\boldsymbol{A}$ and the stream function ϕ. $\boldsymbol{F}_m$ is then expressed in the form

$$\boldsymbol{F}_m = \nabla \times f_m \hat{z} . \quad (5)$$

The spatial structure of the driving term f_m in equation (5) should then be confined to relatively large scales (because of large-scale photospheric forcing), while its temporal profile should be reminiscent of the convective cell origin of the photospheric driver. We have performed numerical simulations with a forcing term f_m of the form

$$f_m = A_1(x, y) \sin^2\left(\frac{\pi t}{2t^*}\right) + A_2(x, y) \sin^2\left(\frac{\pi t}{2t^*} + \frac{\pi}{2}\right), \quad (6)$$

where

$$A_i = \sum_{nm} \alpha_{nm}^i \sin\left(k_n x + k_m y + \zeta_{nm}^i\right) . \quad (7)$$

The wavenumber values k used are all in the range $3 \leq (k_n^2 + k_m^2)^{1/2} \leq 4$. Notice that the forcing term consists of two "eddies" with a turnover time $2t^*$, which are tem-

porally out of phase. At the end of each t^* interval, the terms α^i_{nm} and ζ^i_{nm} are alternately changed randomly (with a uniform distribution over the intervals [0, 1] and [0, 2π], respectively) for the eddy of vanishing amplitude. The α^i_{nm} are then renormalized so that the spatial average of A_i is $\langle A_i \rangle = 1$, implying that the rms spatial nondimensional value for the forcing term f_m is also unity ($\langle f_m \rangle = 1$). The physical units of the model are then fixed in terms of the large-scale magnetic field B_0, the typical photospheric velocity $u_{\rm ph}$ (in units of B_0), the loop length L, and the aspect ratio $1/\epsilon$.

Let us denote the units of magnetic field, velocity, and length used to render our equations nondimensional by b_0 and $l_\perp$, respectively, along with the time unit $\tau = l_\perp/b_0$, hereafter called a time step. A dimensional analysis of equations (2), (3), and (5) then leads to

$$1 \sim \langle f_m \rangle \sim \frac{B_0}{b_0} u_{\rm ph} \frac{\tau}{L} ,$$

and eliminating τ in favor of b_0, $l_\perp$ gives

$$b_0 \sim B_0 \left(\frac{l_\perp u_{\rm ph}}{B_0 L} \right)^{1/2} . \tag{8}$$

The term b_0 is the poloidal Alfvén velocity mentioned in the introduction, and this is the only velocity unit directly relevant to our simulations, since the axial field does not appear in the equations. Assuming that the photospheric velocity satisfies $u_{\rm ph} \simeq 0.001 B_0$, and assuming a value of $1/\epsilon = 10$ for the loop-aspect ratio, we obtain from equation (8)

$$\frac{b_0}{B_0} \simeq 0.01 , \quad \tau \simeq 10 \frac{L}{B_0} \, \mathrm{s} . \tag{9}$$

If $B_0 \simeq 1000$ km s^{-1} and $L \simeq 10^4$ km, τ turns out to be $\tau \simeq 100$ s. Our numerical domain is a square lattice with periodic boundary conditions. We have performed a series of simulations with a resolution of 128×128, $\tau^* = 16\tau$, extending from $t = 0$ up to $t = 4100$, that is, $\sim$114 hr real coronal time with the choice of constants given above. As a result, we have achieved time stationarity (a "flare" occurring does not imply a significant impact on the total energy that has been dissipated until the time of its occurrence). Resistivity and viscosity are adapted to the grid (in the case of a 128×128 resolution, the value used is $\eta = \nu = 0.01$). In addition, we have performed a limited number of higher resolution runs, using a lattice with dimensions 256×256 (the value of the resistivity used in this case is $\eta = \nu = 0.004$). The latter data set will be used mostly for statistical analysis in space, while an analysis of the temporal evolution of the system will be carried out for the lower resolution.

3. TEMPORAL EVOLUTION AND SPATIAL STRUCTURE

In this section we discuss the statistical analysis performed on the data representing both the time evolution and the spatial structure of the model introduced above.

In Figure 1*a* we show the time evolution of the current dissipation averaged over the whole system, $E_D = \langle \eta J^2 \rangle$. The time series is characterized by a high level of intermittency, with an order of magnitude variation of the dissipated energy over short timescales. Intense dissipative events occur well above a continuous active background of small-scale flickering. In order to quantitatively define a dissipative event, we must apply an adequate method of

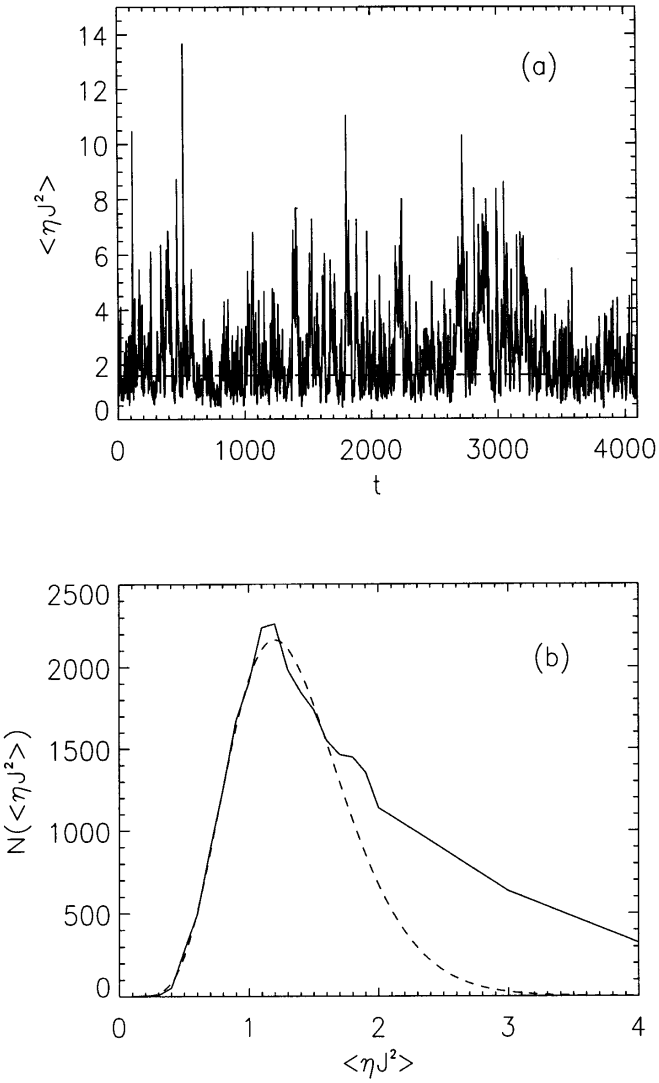

FIG. 1.—(*a*) Time evolution of the average current dissipation. Dashed line corresponds to the temporal noise threshold. (*b*) Low-energy part of the $\langle \eta J^2 \rangle$ distribution function (*solid line*) and the best χ^2 fit obtained (*dashed line*).

noise reduction; in particular, we must define a threshold that allows us to define the beginning and end of an event. For this reason, the data plotted in Figure 1*a* have been used to build up a discrete distribution function of the dissipated power over the entire time series. The technique used to derive the distribution function from the data is described in the Appendix. The resulting distribution function, restricted to its low-energy band to clearly demonstrate the features of the noise present in the time series, is shown by the solid line in Figure 1*b*. The noise component is well represented by a χ^2 distribution function of the form

$$N(x) = \frac{C}{2\Gamma(n/2)} \left(\frac{x}{2} \right)^{n/2-1} \exp\left(-\frac{x}{\sigma} \right) , \tag{10}$$

where $x \equiv E_D$, $\Gamma(n/2)$ is the Gamma function, n is the number of degrees of freedom, and C and σ are the fitting constants. The best fit for our time series is obtained for $n = 17$ (Fig. 1*b*, *dashed curve*). The χ^2 confidence level of the fit is close to 100%. For $E_D \geq E_n = 1.6$, the measured distribution function begins to deviate significantly from the χ^2 fit; such a value can therefore be taken as the temporal

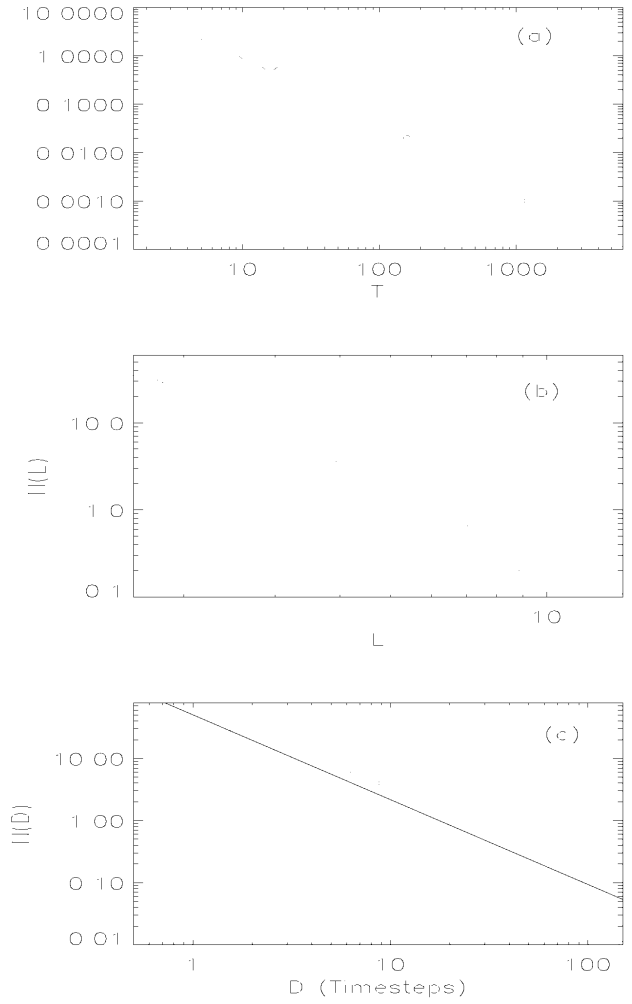

FIG. 2.—Scaling laws for the average current dissipation. Straight lines show the least-square power-law fits. (*a*) Total energy content. (*b*) Peak activity. (*c*) Duration of the events.

noise threshold of the average current dissipation time series. The threshold is also shown in Figure 1*a* (*dashed line*).

After having subtracted the noisy background of the time series, we are able to identify a total of 369 discrete events for the average current dissipation. By means of the relationship between our time step and real time (eq. [9]), one may notice that we have recorded a mean number of events above noise of about 3.2 hr^{-1}.

The distribution functions of the total energy content, peak activity, and duration of such events are plotted in Figures 2*a*, 2*b*, and 2*c*, respectively. Although there is some dispersion in the data, the distribution functions of duration and total energy content may be represented by robust power laws extending over 2–2.5 orders of magnitude. Notice that we obtain events that last from ~ 1.6 minutes ($\sim 1\tau$) up to ~ 4.1 hr (150τ). The distribution function of the

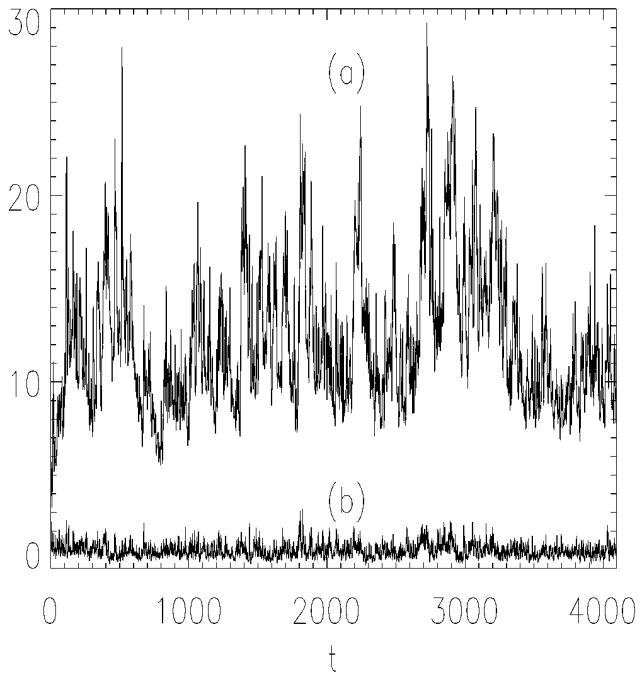

FIG. 3.—Time series of (*a*) the average magnetic energy and (*b*) the average kinetic energy.

peak activity displays a power law over 1 order of magnitude. The reason for this is that the maximum current that can be obtained in the integration box is limited by the spatial resolution and decreases with increasing resistivity.

The scaling indices of the distribution functions, namely δ_T (for total energy content), δ_L (for peak activity), and δ_D (for duration), as well as the respective mean absolute deviations, the noise threshold E_n, and the average and maximum values $(S/N)_{av}$, $(S/N)_{max}$ of the signal-to-noise ratio are provided in Table 1. The average power dissipated in all events above noise is smaller than the average power dissipated in the background [$(S/N)_{av} \simeq 1.878$], which again is related to the fact that no large "flare" occurs during our time series.

Notice that the scaling index for total energy content ($\delta_T \simeq -1.32$) is larger than the scaling index for peak activity ($\delta_L \simeq -2.81$), which means that the peak-activity frequency distribution is much steeper than the total energy content distribution. We will come back to this point in the final section.

In Figure 3 we present the time evolution of both the magnetic energy (Fig. 3*a*) and the kinetic energy (Fig. 3*b*) averaged over the whole system; the kinetic energy is practically negligible, as expected since the forcing acts only on the magnetic field. However, as we will show later, the velocity can increase considerably locally with respect to its average value, exceeding the poloidal Alfvén velocity in jet-type structures at the end of current sheets.

It is interesting to note that input power presents varia-

TABLE 1

TEMPORAL NOISE THRESHOLDS AND SCALING INDICES

Case	E_n	$(S/N)_{av}$	$(S/N)_{max}$	δ_T	δ_L	δ_D
$\langle \eta J^2 \rangle$.....	1.6	1.878	8.539	-1.32 ± 0.24	-2.81 ± 0.11	-1.36 ± 0.19
ηJ^2_{max}	320.	1.134	47.96	-1.27 ± 0.08	-2.30 ± 0.08	-2.73 ± 0.22

tions of the same order of magnitude and occurring on the same timescale as the dissipated power and the total energy content. This feature is due to the fact that the forcing term for the magnetic energy presents a coupling between $\boldsymbol{F}_m(x, y, t)$, which is a smooth function of both time and space, and the magnetic field $\boldsymbol{b}_\perp$, which on the contrary is highly structured. This coupling accounts for the fact that no matter what forcing term is used in the Faraday equation, the input power is a strongly fluctuating function of both space and time.

Let us now discuss in detail the spatial structure that arises as a result of the external forcing. We have analyzed two time intervals of 24τ, corresponding to different levels of activity in terms of energy dissipation, using higher resolution configurations (grid dimensions 256×256). The time evolution of $\langle J^2 \rangle$ is shown by the solid lines in Figure 4*a* for the time interval $T1$, corresponding to $2750\tau < t < 2774\tau$, and in Figure 4*b* for the time interval $T2$, corresponding to $2602\tau < t < 2626\tau$. The integration in each time interval is performed using the corresponding configuration obtained in the time series at low resolution as an initial condition (fields have been bilinearly interpolated to yield a 256×256 initial condition). Inspection of Figures 1*a* and 4 reveals that the time series are different at different spatial resolutions.

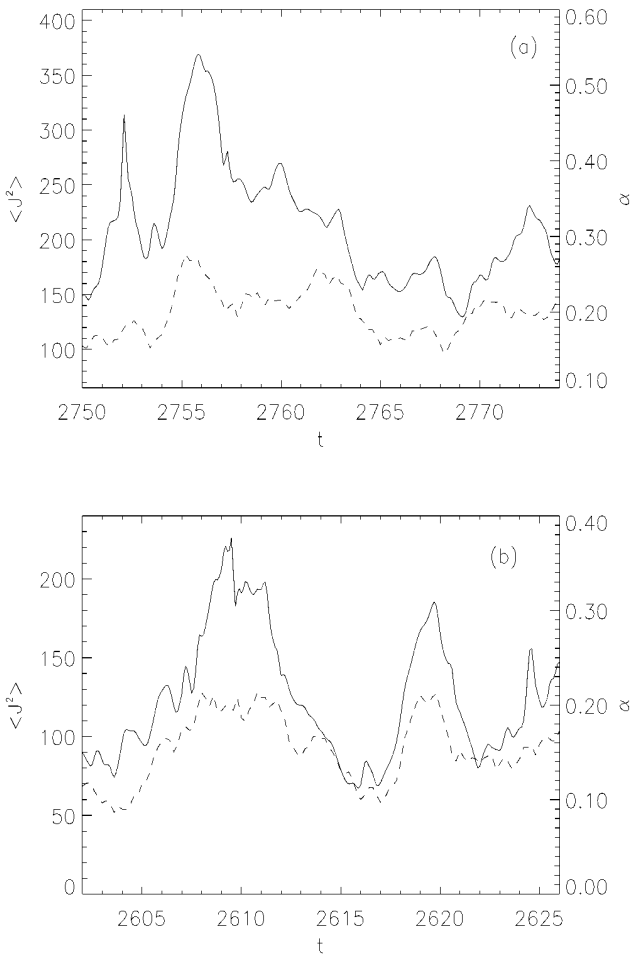

FIG. 4.—Time evolution of the square current density (*solid line*) and surface filling factor (*dashed line*) for high-resolution (256×256) spatial configurations referring to: (*a*) time interval $T1$ starting at $t = 2750\tau$; (*b*) time interval $T2$ starting at $t = 2602\tau$.

In Figures 5 (Plate 19) and 6 (Plate 20) we show some features of the evolution of spatial structures on short timescales. The sequence of six frames in each figure corresponds to a total time interval of 1.2τ (approximately 120 s real time) in Figure 5 (Plate 19) and 2.4τ in Figure 6 (Plate 20). In each frame we show the spatial structure of the current density in two-dimensional images (*bottom panel*) and in the surface plots (*middle panel*). The contour lines in the top panel refer to the vector potential contour lines and correspond to the field lines of the poloidal magnetic field $b_\perp$. We notice that in both the high- and low-activity time intervals the overall dynamics is dominated by an inverse cascade of the vector potential, so that although the forcing contains three to four randomly oriented eddies, the magnetic structure aligns coherently along any one axis of the numerical domain (Einaudi et al. 1996). The trend of the system is therefore to organize itself into well-defined magnetic loops (in the two-dimensional cross section the loops appear as islands) separated by narrow localized current sheets where intense dissipation episodes occur. Current sheets (filaments in our two-dimensional images) can be identified as brightenings in the two-dimensional images (*bottom*) and narrow spikes extending well above the average current density in the surface plots (*middle*); their position can also be detected in the magnetic field contour lines, which clearly indicate the presence of one or more X-points. The typical lifetime of those current sheets is on the order of the dynamical timescale ($\sim 0.1\tau$).

The main difference between periods of high (Fig. 5; [Pl. 19]) and low (Fig. 6; [Pl. 20]) activity appears to be the presence in the high-activity regime of a current loop that is sustained throughout the period of observation by the overall dynamics. The current loop makes an appreciable contribution to the dissipation. In all periods, small-scale current sheets appear to be the sites of magnetic reconnection, which occurs on the dynamical timescale and is driven by the interaction of at least two magnetic islands. This phenomenon is well represented in the sequence shown in Figure 6 (Plate 20), where the magnetic island on the right in the magnetic field line plot travels toward the bigger island on the left, while a thin current sheet is formed in front of it. The two islands are separated by an X-point, which disappears in the frame (Fig. 6*e*; [Pl. 20]), whereas the current sheet seems to be dissipated 0.4τ later in frame (Fig. 6*f*; [Pl. 20]). Notice that simultaneously with the interaction of the two islands, current sheets appear sporadically in various locations throughout the system, indicating the possible presence of a nonlocal communication process between dissipating (or "flaring") sites. The phenomenon exemplified above is typical of the dynamics occurring at all times, and in fact it can be seen in the sequence shown in Figure 5 (Plate 19) as well. We have focused on the right-hand side of the frames, in which the formation, evolution, and disruption of an intense current sheet is evident. In Figure 7 we present snapshots of the local structure of the magnetic field (Fig. 7*a*), current density (Fig. 7*b*), velocity field (Fig. 7*c*), and vorticity (Fig. 7*d*). A current sheet appears clearly in the center of the frame, with a maximum value in system units of 82.98, almost 1 order of magnitude higher than the spatial noise threshold defined below. The maximum value attained by the magnetic field in the box is $14.53 b_0$, much smaller than the large-scale magnetic field B_0 we assume to exist in the z-direction. From an inspection of the velocity and vorticity structure, it appears that recon-

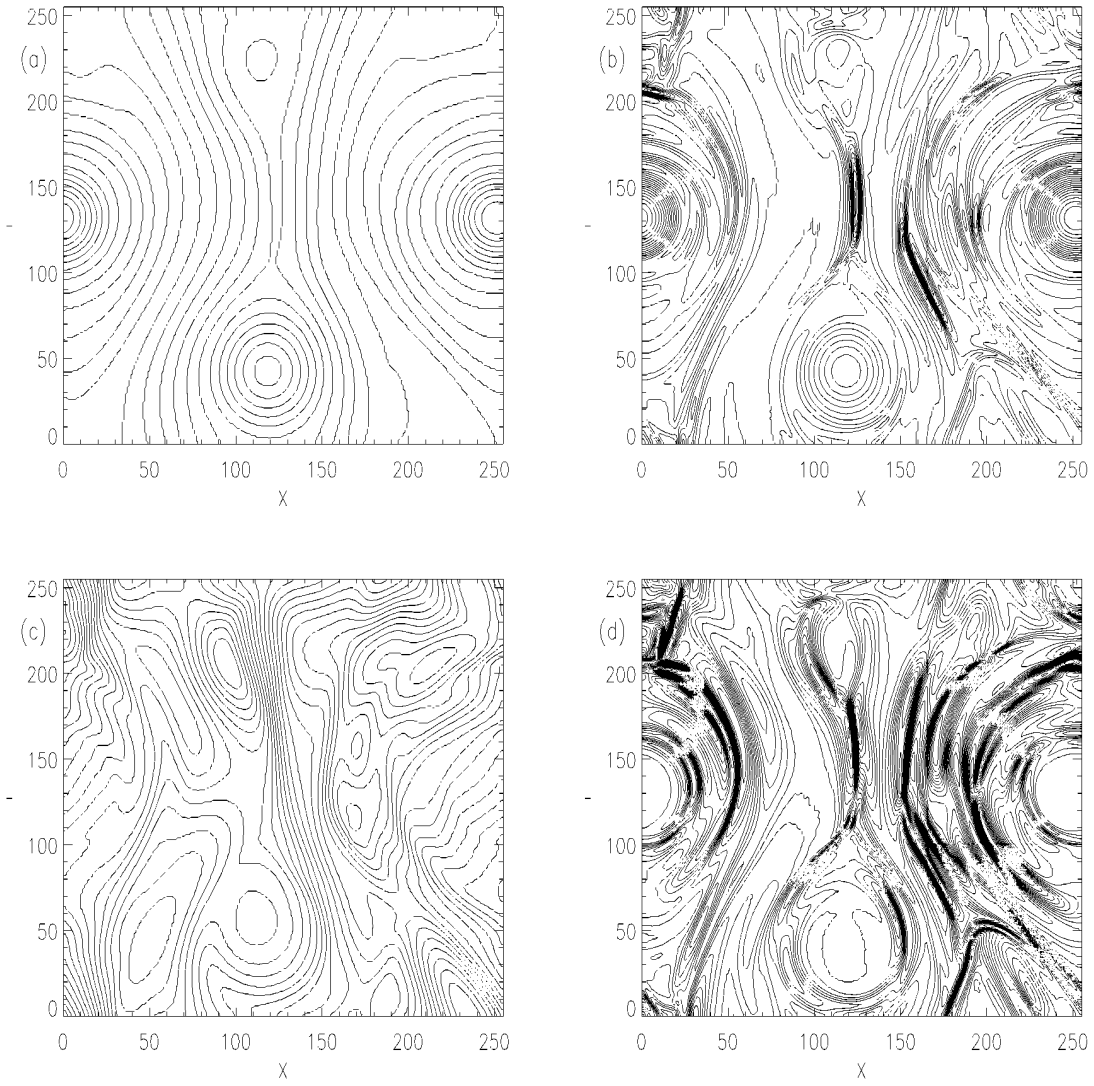

FIG. 7.—Snapshots at $t = 2753.2\tau$ of a high-resolution spatial configuration showing (*a*) magnetic field, (*b*) current density, (*c*) velocity field, and (*d*) vorticity.

nection is taking place within the current sheet and that reconnection is the mechanism responsible for its disruption. In fact, we observe jets outflowing along the sheet with the typical quadrupole structure of the vorticity. The maximum value of the velocity in poloidal Alfvén velocity units is 2.41 inside the jet, whereas the average velocity throughout the grid is 0.95. The maximum velocity is therefore higher than average and much higher than the assumed photospheric velocity, which in our units is 0.1. It is therefore smaller by almost 1 order of magnitude than the maximum poloidal Alfvén velocity in the box, but exceeds the local value of the poloidal Alfvén velocity around the current sheet.

In order to carry out a statistical analysis of the spatial configurations, we must construct, in a fashion analogous to that of the time series, a distribution function of spatial dissipation events, i.e., the distribution function of sites with a given current J as a function of J. To increase the size of the data set, we have chosen to include data from 120 configurations of the current density in the high-resolution 256×256 run, the corresponding time interval being 24 time steps (ranging from $t = 2750\tau$ to $t = 2774\tau$; we collected the spatial configurations every 0.2τ, that is, five configurations per time step). This may be justified on the grounds of the statistical homogeneity of our sample; we assume the 120 spatial configurations at different times to be equivalent, statistically, to a spatial region of 120 times greater area taken at one instant. The resulting distribution is shown in Figure 8*a*. For low values of J, the distribution is well fitted by a Gaussian component of the form

$$N(x) = C_1 \exp\left[-\frac{(x - C_2)^2}{\sigma^2}\right], \tag{11}$$

where $x \equiv J$ and C_1, C_2, and σ are the fitting constants (Fig. 8*a*, *dashed line*). For larger values of $J(\geq 9)$, the distribution diverges from the white noise (Gaussian) component, and we therefore use this value to define a threshold for spatial events. It should be noted at this point that noise threshold derivations can also be obtained from the spatial configurations of magnetic fields, velocity fields, and vorticities. Since, however, we are mostly interested in energy dissipation through Ohmic heating, we shall restrict our analysis to currents.

After having subtracted the background from the spatial current structures, we may again construct the distribution

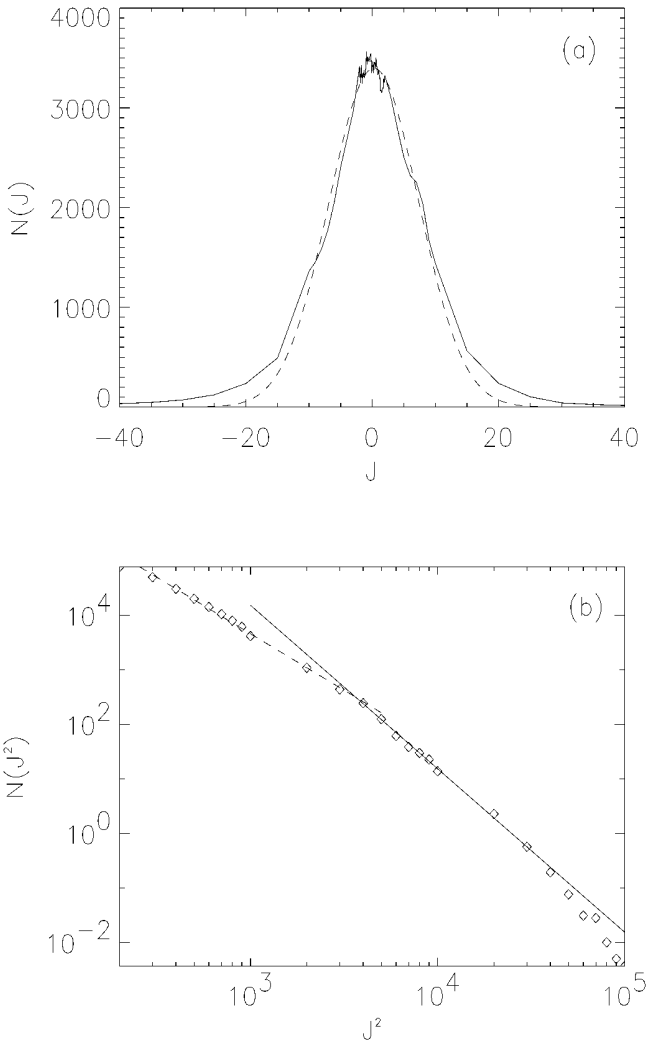

FIG. 8.—Statistics in space for high-resolution (256 × 256) spatial configurations. (*a*) Spatial distribution function of the current density (*solid line*) and Gaussian best fit (*dashed line*). (*b*) Scaling law for the square current density above noise. Straight and dashed lines show the least-square power-law fits in the low- and high-energy ranges.

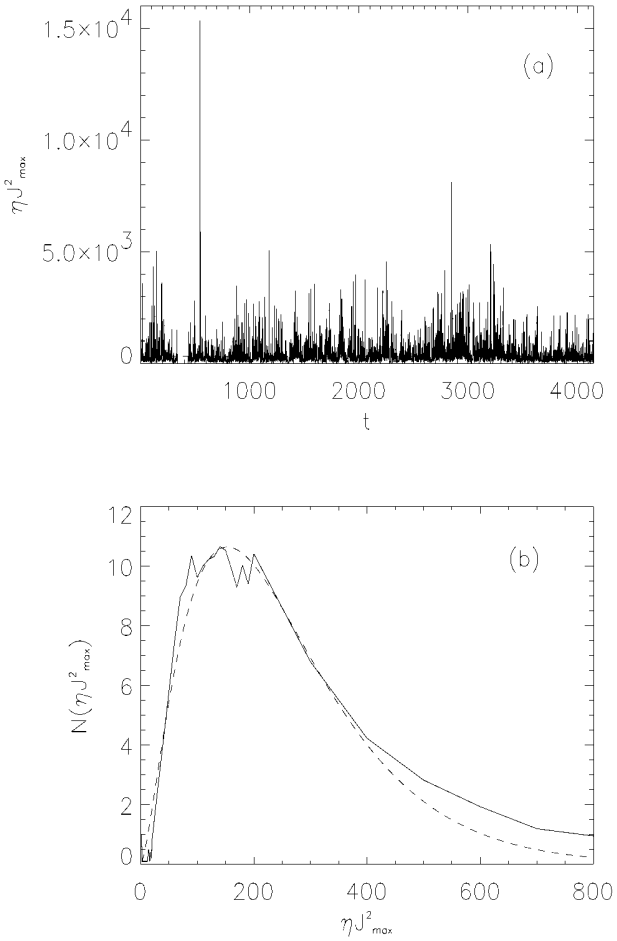

FIG. 9.—(*a*) Time evolution of the maximum current dissipation. Dashed line corresponds to the temporal noise threshold. (*b*) Low-energy part of the $\eta J^2_{\max}$ distribution function (*solid line*) and the best χ^2 fit obtained (*dashed line*).

function of their magnitudes. We have plotted in Figure 8*b* the distribution function of J^2, with J denoting the current densities that extend above the noise. It is evident that most of the data can be fitted by two power laws with different scaling indices, namely, $\delta_1 \simeq -2.07 \pm 0.05$ for small values of J^2 and $\delta_2 \simeq -2.61 \pm 0.21$ for higher values. The power law in the low-energy range of the distribution is flatter than that in the high-energy range. The existence of such a component could be due to poor spatial resolution and therefore may not be particularly meaningful.

Since we have determined the noise threshold for spatial currents, it is of interest to provide an estimate for the surface filling factor α, defined as the ratio between the area occupied by the currents above threshold and the total area of the integration box. The quantity α can be directly compared with the analogous quantity f, obtained from observations, defined as the fraction of the observed volume that radiates strongly in a particular waveband because of either a different density or a different temperature from its surroundings.

In Figure 4 we show, as already mentioned, the temporal profile of $\langle J^2 \rangle$ (*solid lines*) for two time intervals of 24τ at high resolution. The dashed lines in the same figure show the temporal profile of the filling factor α over the same time intervals. Its value ranges roughly between ~ 0.1 and ~ 0.3 and seems to be fairly well correlated with the average dissipated power. We notice that when the dissipated power peaks, the filling factor seems to saturate at a certain level until the dissipated power reduces again. This implies that a sharp increase of activity occurs as a result of a local increase in the current rather than because of broadening or an increase in the number of current sheets.

So far, we have investigated the average dissipation properties and the spatial distribution of currents over limited intervals of time. One time series that combines the two kinds of information is that for the maximum current (which would correspond to the maximum photon count in an individual pixel over the whole field of view as a function of time); in Figure 9*a* we illustrate the time series of the maximum current dissipation $\eta J^2_{\max}$ for each time instant 0.1τ. Since $J_{\max}$ corresponds to the maximum current density within the spatial configuration at a given instant, it does not correspond to the temporal profile of a single current sheet, but rather may appear at current sheets in different locations at different instants (see for example the surface plots of Figs. 5 and 6; [Pls. 19–20]). We have used

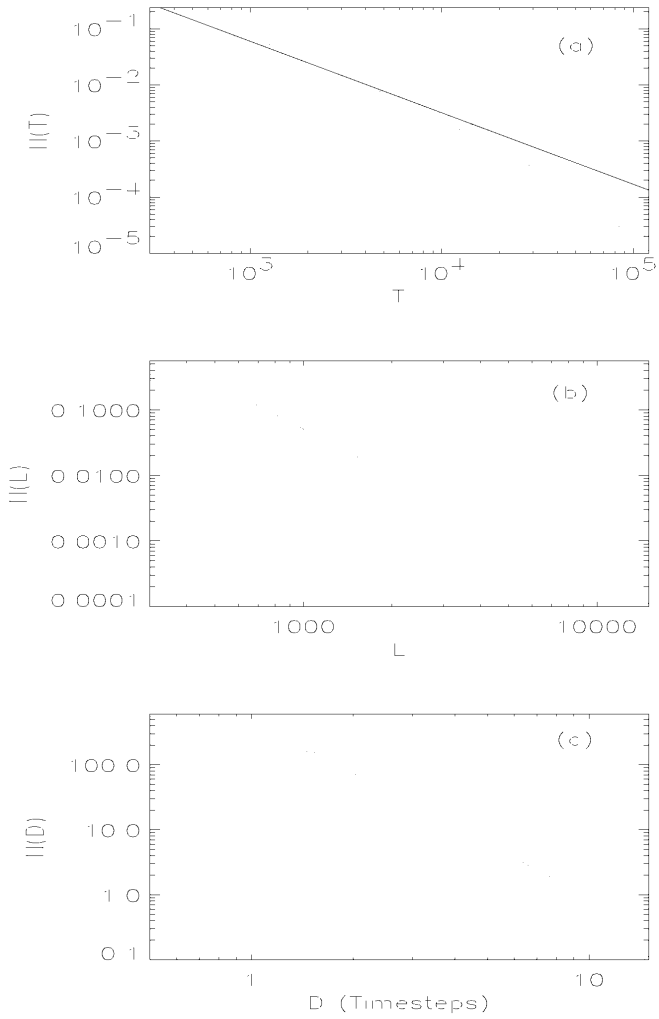

FIG. 10.—Scaling laws for maximum current dissipation. Straight lines are the least-square power-law fits. (*a*) Total energy content. (*b*) Peak activity. (*c*) Duration of the events.

the same method, as in the case of the average dissipation power, to extract the noise threshold. The low-energy band of the resulting distribution function is provided in Figure 9*b*. The noise component may again be well represented by a χ^2 probability function in the form of equation (10), for which we now consider $x \equiv \eta J^2_{\max}$. The best fit occurs for $n = 5$, represented by the dashed curve of Figure 9*b*. The noise threshold in this case is roughly estimated to be $E_n \simeq 320$, shown by a (not easily observed) dashed line in Figure 9*a*.

Subtraction of noise in the time series originates a total of 1950 discrete events (that is, a mean number of events approximately equal to 17.1 hr^{-1}). The significant difference between this number and that of the average-dissipation events is, of course, due to the fact that the peaks shown in Figure 9*a* correspond to dissipation in single current sheets, where we have not applied an averaging process.

The distribution functions of events derived from the instantaneous maximum current dissipation are given in Figure 10*a* for the total energy content, in Figure 10*b* for peak activity, and in Figure 10*c* for the event duration. Again, one notices that noise reduction has led to the emergence of power laws, although their extent is slightly reduced as compared to those determined from the average dissipation (Fig. 2). The noise threshold E_n, the average and maximum values of the signal to noise ratio [$(S/N)_{\mathrm{av}}$ and $(S/N)_{\max}$, respectively], and the values of scaling indices for the total energy content, the peak activity, and the duration (δ_T, δ_L, and δ_D, respectively) for the time series of Figure 9*a* are also given in Table 1. Notice that, on the average, maximum dissipation peaks are also barely above noise, i.e., $(S/N)_{\mathrm{av}} \simeq 1.134$, although in some cases we obtain dissipative events well above the threshold [$(S/N)_{\max} \simeq 47.96$]. The value of the total energy scaling index is quite similar to that obtained from the average-dissipation time series (within the error bars), while the scaling index of peak activity is rather lower (in absolute values) than the corresponding index from the average-dissipation time series. The distribution function of the events' durations, on the other hand, is significantly steeper than in the first case. Comparing Figures 2*c* and 10*c*, we notice that the maximum-dissipation events are significantly less extended in time [ranging from ~ 10 s (0.1τ) to ~ 300 s (3τ)], indicating that the behavior of maximum dissipation is in fact much more intermittent than average dissipation. This difference should be expected, since we obtain a much larger number of maximum-dissipation than average-dissipation events.

4. CONCLUSIONS AND DISCUSSION

We have performed a statistical analysis of data obtained from an MHD simulation that models the energy-release process in a two-dimensional cross section of a solar coronal loop. By concentrating on the overall long-time behavior of the system, we have shown that magnetically forced MHD turbulence results in an energy release with properties analogous to those observed in the solar corona, namely, the presence of distinct bursts that follow well-defined power laws for total energy content, duration, and peak luminosity. We have also shown that such bursts correspond to forced reconnection in localized current sheets, and that such bursts are associated with bipolar jets in which the plasma is accelerated to the (poloidal) Alfvén speed (see Innes et al. 1997 for observational evidence of such jets seen with *SOHO*), even though the average kinetic energy remains negligible compared to the magnetic energy.

The values of the scaling indices we have found should be taken *cum grano salis*. Resistivity and viscosity are adapted to the grid, and our resolution is fairly poor, so extrapolation from our data, obtained with $\eta = 0.01$, to much lower values is unwarranted. The effect of varying the resolution and the Reynolds number was investigated in Einaudi et al. (1996), where simulations with resolutions of 64×64, 128×128, and 256×256 were reported. There was both a qualitative and a quantitative difference in the temporal profiles for the lower and intermediate resolutions (see Fig. 1 of that paper), while the difference between the intermediate and higher resolution was mostly quantitative, thus providing an indication of the existence of a hypothetical asymptotic "large Reynolds number" evolution.

The interest of the present results lies in the demonstration of the existence of power laws in the coronal response to the photospheric driver, even though the values of the scaling indices will most probably vary significantly with increasing resolution. Another limitation of our results, as mentioned in the Introduction, arises from the two-

dimensional nature of our simulations. Within this model it is impossible to store significant amounts of energy in the system, as the turbulent cascade dissipates any input power in an efficient way. In a truly three-dimensional system, magnetic helicity is also injected into the system; global conservation properties associated with minimum-energy states at given helicity offer much greater possibilities for the dynamics that are probably necessary to describe large-scale energy release manifestations in the sun. One should therefore be cautious when comparing the scaling indices resulting from our simulations with those derived from observational data that refer to events involving topologically complex magnetic structures. On the other hand, it is also wrong to extrapolate the results obtained for the highly energetic flares to much lower energies and smaller scales, where the influence of the three-dimensional magnetic topology is unclear and a description in terms of simple loops is more realistic; in fact, observations of type I bursts reveal a much steeper distribution function with a power-law index close to -3 (Mercier & Trottet 1997).

With the caveats given above, it is interesting to remark on the scaling index of the spatial dissipation power law ($\delta \simeq -2.61$) obtained in § 3. This results from an analysis of the spatial structures of more than 100 configurations obtained with the highest resolution used and therefore reflects details of a large number of highly localized (in space and time) energy-release episodes. We expect the absolute value of this index to become larger (i.e., steeper) with increasing resolution because of the enhanced capacity for describing smaller scales. This value is about twice the value of the indices arising from the temporal evolution of the spatially averaged dissipation and of the maximum dissipation, and this experimental fact may give some insight into the question of coronal heating via nanoflares. If we interpret the average dissipation in our simulation in terms of events in the same way observers do, the extrapolation below a given energy may lose meaning, since the spatially averaged output over a given region may never fall below a given value, so that a higher spatial resolution is necessary to define and pick up low-energy events. On the other hand, our spatial statistics show precisely that the number of events at small energies does increase considerably with decreasing energy, providing indirect evidence in favor of the nanoflare scenario.

In our two-dimensional simulations, magnetic structures exhibit a tendency to self-organize in space and time. Generally speaking, such self-organization relies on the creation of a relatively small number of large-scale, well-defined magnetic structures, with small-scale current sheets at their boundaries. In the more general three-dimensional case, the dynamics of the system must also depend on its capacity to store magnetic energy at large scales, but the release still occurs in the current sheets that form and disrupt on the dynamical timescale, since the local magnetic Reynolds number is of order 1 on the current sheet scale. In order to model coronal phenomena such as large two-ribbon flares, compact-loop flares, bright points, flashes, or explosive events down to coronal heating, it would be necessary to simulate the associated magnetic topology by adopting very large Reynolds numbers. It is, however, currently impossible to perform three-dimensional runs with the resolution and length of the two-dimensional experiments carried out in this paper; therefore, to proceed in modeling such phenomena it is paramount to investigate possible similarities between our simulations and existing statistical theories. One candidate concept seems to be that of self-organized criticality, or SOC (Lu & Hamilton 1991; Lu at al. 1993; Vlahos et al. 1995; Galsgaard 1996), whose basic feature is the non-Gaussianity of the response obtained from a purely Gaussian driver, together with self-similarity and scale invariance. SOC systems are discrete and become self-organized after being driven toward a statistically marginally stable state, the route to this state being defined by the existence of instability criteria that, translated to MHD, loosely imply a critical value of current density. Disruption of current sheets and subsequent energy dissipation occurs when the localized current density crosses a critical threshold. It has recently been shown that the SOC state survives even with large variations of the driver, provided that its average value remains small compared to the threshold (Georgoulis & Vlahos 1996, 1998). We believe that certain refinements could be introduced in SOC models (e.g., in the nature of the driver and the critical threshold) to better allow SOC to fit with the continuous MHD model. Specifically, the results presented in this study introduce some questions as to whether the critical threshold should be defined only in terms of localized current densities, or whether the spatial scale of instabilities should be introduced as well. Figure 5 (Plate 19) shows that significant current concentrations may well appear in relatively extended spatial scales, without, however, giving rise to impulsive dissipation. On the contrary, dissipation through magnetic reconnection originates from gradients at the smallest spatial scales, triggered mostly by the presence of localized strong current sheets. This feature is clearly seen in the intense, point-like brightenings and sharp impulses in the images and surface plots of Figures 5 and 6 (Plates 19–20; see for example Fig. 6*d*). In any case, the detailed derivation of a SOC-type model from MHD equations remains an important open problem, which we hope to pursue in the future.

We would like to thank A. Pouquet and C. Chiuderi for many useful and stimulating discussions. Numerical simulations have been performed on the Cray facilities of ENEL (Pisa, Italy). This work has received partial support from the Greek State Foundation for Scholarships (IKY) and the EEC program ERASMUS.

APPENDIX

All distribution functions $N(x)$ have been obtained in the following way. We use a variable bin size, which increases by an order of magnitude every time the x-value changes by an order of magnitude. The minimum bin size used, corresponding to the interval $0 < x < 100$, is $b_{\min} = 10$. The occurrence frequency N of a given value $\bar{x}$ is obtained by counting the number of times a value of x contained in the bin corresponding to $\bar{x}$ occurs in the time series, and by renormalizing this number with the minimum bin size, i.e., multiplying by $b_{\min}/\bar{b}$, where $\bar{b}$ is the bin size corresponding to $\bar{x}$. This procedure is used to determine the distribution functions for J, J^2, and $J^2_{\max}$.

The distribution functions for the dissipated power are derived from those for J^2 and $J^2_{\max}$, transforming the intervals of x and the corresponding bin sizes according to the value of η ($x \to \eta x$ and $b \to \eta b$).

REFERENCES

Berger, M. A. 1991, A&A, 252, 369
Biesecker, D. A. 1994, Ph.D. thesis, Univ. New Hampshire
Crosby, N. B., Aschwanden, M. J., & Dennis, B. R. 1993, Sol. Phys., 143, 275
Démoulin, P., Hénoux, J. C., & Mandrini, C. H. 1994, A&A, 285, 1023
Dennis, B. R. 1985, Sol. Phys., 100, 465
Dmitruk, P., & Gómez, D. O. 1997, ApJ, 484, L83
Einaudi, G., Velli, M., Politano, H., & Pouquet, A. 1996, ApJ, 457, L113
Galsgaard, K. 1996, A&A, 315, 312
Galsgaard, K., & Nordlund, A. 1996, J. Geophys. Res., 101, 13445
Georgoulis, M. K., & Vlahos, L. 1996, ApJ, 469, L135
———. 1998, A&A, in press
Hendrix, D. L., & Van Hoven, G. 1996, ApJ, 467, 887
Hudson, H. S. 1991, Sol. Phys., 133, 357
Innes, D. E., Inhester, B., Axford, W. I., & Wilhelm, K. 1997, Nature, 386, 811
Lin, R. P., Schwartz, R. A., Kane, S. R., Pelling, R. M., & Hurly, C. C. 1984, ApJ, 283, 421
Longcope, L., & Sudan, L. 1994, ApJ, 437, 491
Lu, E. T., & Hamilton, R. J. 1991, ApJ, 380, L89
Lu, E. T., Hamilton, R. J., McTiernan, J. M., & Bromund, K. R. 1993, ApJ, 412, 841
Mercier, C., & Trottet, G. 1997, ApJ, 474, L65
Mikic, Z., Schnack, D. D., & Van Hoven, G. 1989, ApJ, 338, 1148
Parker, E. N. 1972, ApJ, 174, 499
———. 1983, ApJ, 264, 642
———. 1988, ApJ, 330, 474
———. 1989, Sol. Phys., 121, 271
———. 1991, ApJ, 372, 719
Pearce, J., Rowe, A. K., & Yeung, J. 1993, Ap&SS, 208, 99
Pick, M., Klein, K. L., & Trottet, G. 1990, ApJS, 73, 225
Ramaty, R., & Murphy, R. J. 1987, Space Sci. Rev., 45, 213
Strauss, H. 1993, Geophys. Res. Lett., 20, 325
Strauss, H. R. 1976, Phys. Fluids, 19, 134
———. 1977, Phys. Fluids, 20, 1354
Sturrock, P. A., & Uchida, Y. 1981, ApJ, 246, 331
Van Ballegooijen, A. A. 1986, ApJ, 311, 1001
Vilmer, N. 1987, Sol. Phys., 111, 207
Vlahos, L., Georgoulis, M., Kluiving, R., & Paschos, P. 1995, A&A, 299, 897